J. Electroanal. Chem., 238 (1987) 9–31
Elsevier Sequoia S.A., Lausanne – Printed in The Netherlands

CURRENTS IN THIN LAYER ELECTROCHEMICAL CELLS WITH SPHERICAL AND CONICAL ELECTRODES

JOE M. DAVIS, F.-R.F. FAN and A.J. BARD *
Department of Chemistry, University of Texas at Austin, Austin, TX 78712 (U.S.A.)
(Received 13th July 1987)

ABSTRACT

Thin layer electrochemical cells in which the electrodes are two hemispheres, a hemisphere and a plane, two cones, a cone and a plane, and crossed cylinders, are considered. An approximate procedure was used to derive analytical expressions for the steady-state, diffusion-limited current at these cells. The procedure rests on the assumption that the diffusive flux of electroactive species in the cell is largest in the region of minimum electrode separation and is approximately one-dimensional. This assumption was tested by calculating from the continuity equation and Fick's first law, the current attributable to the full three-dimensional flux of a redox couple to the electrodes of a simple model cell formed from two axially aligned hemispheres. The results show that the one-dimensional-flux approximation is a good one at short separation distances.

INTRODUCTION

This paper discusses the current–distances behavior of electrochemical thin layer cells with electrodes of spherical and conical shape. Twin-electrode thin layer cells conventionally employ planar parallel electrodes spaced about 50–100 μm apart [1]. When a redox couple, Ox/Red, is introduced into the interelectrode gap and the potential between the electrodes adjusted so that diffusion-limited redox processes occur, a steady-state current, i, that varies with $1/l$ (where l is the interelectrode separation) flows. We have recently become interested in ultrathin-layer cells with interelectrode spacings on the nm level [2]. To avoid problems with maintaining the electrodes in a parallel configuration at these small distances, the electrodes have a cylindrical shape and are oriented perpendicular to one another (i.e., in the crossed-cylinder arrangement shown schematically in Fig. 1). In such a configuration only a single contact area (with smooth electrodes) is achievable. An approxi-

* To whom correspondence should be addressed.

0022-0728/87/$03.50

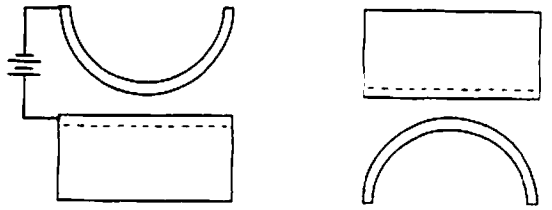

Fig. 1. Orthographic schematic of ultrathin-layer crossed-cylinder cell.

mate treatment of the steady-state current–distance behavior in such a cell showed that, unlike planar electrode cells, the current became independent of interelectrode spacing at short distances [2]. Other electrode configurations that have similar single area contact properties involve spherical and conical electrodes, and we describe here the behavior of thin layer cells based on these electrode geometries (see Fig. 2).

Three coordinates are required to describe mathematically these electrode surfaces, and the diffusion layer consequently grows from them in three dimensions. At any

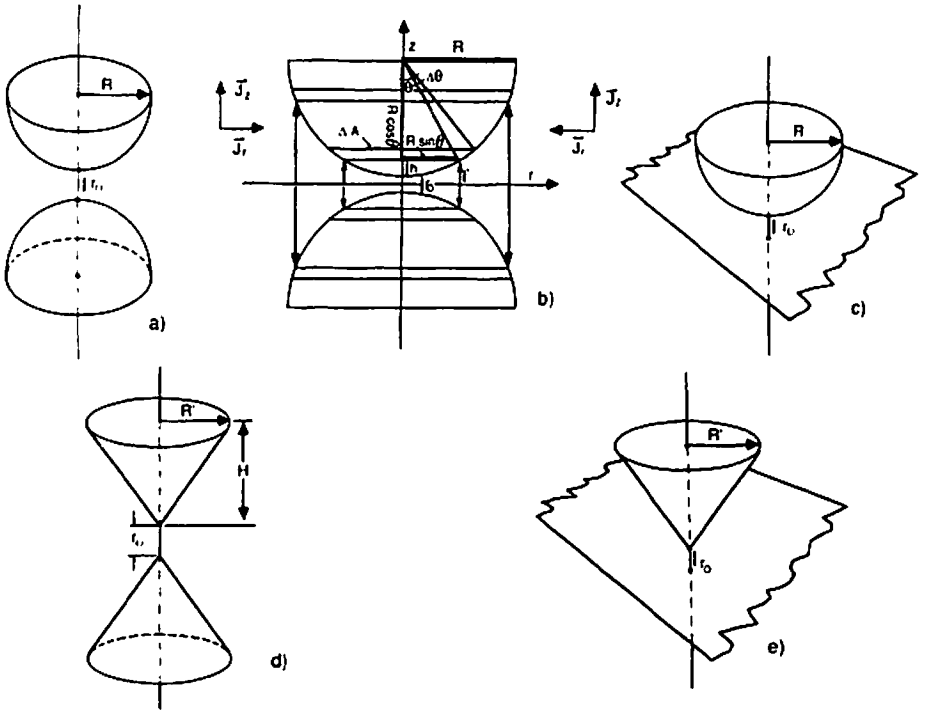

Fig. 2. Thin layer cells. (a) Twin hemispherical cell. (b) Model for twin hemispherical cell. Flux J_z parallels the z axis and is confined between area strips approximating parallel-plate electrodes. Flux J_r from surrounding solution is ignored. (c) Hemisphere/plane cell. (d) Twin conical cell. (e) Cone/plane cell.

interelectrode separation, therefore, species can diffuse into the interelectrode gap from the bulk solution. If the separation is very small, however, the concentration gradient in the small interelectrode gap is much greater than that at the peripheral electrode edges. Because the diffusive current is proportional to this gradient at the electrodes surface, in accordance with Fick's first law, the cell current is highly localized within this narrow-gap region and, to a first approximation, arises from a one-dimensional flux of the redox couple in this region to and from the electrodes. Various expressions for the steady-state current for different electrode geometries are derived below with this approximation.

It is important, however, to assess the accuracy of the one-dimensional-flux approximation used to derive these simple analytical equations. The validity of the approximation was investigated by calculating from the continuity equation, the full three-dimensional flux of a redox couple to the electrodes of a relatively simple thin layer cell, one that is formed from two axially aligned conductive hemispheres facing one another as shown in Fig. 2a. From the flux the diffusion-limited current generated by this twin hemispherical cell was determined and compared to that based solely on a one-dimensional flux. The results indicate that the one-dimensional-flux approximation is a good one for this cell at short separation distances. Its applicability to cells based on different geometries is also discussed. Other electrochemical cells and configurations based on closely spaced electrodes, e.g., parallel planar electrodes, have been described elsewhere [3,4].

EQUATIONS BASED ON ONE-DIMENSIONAL-FLUX APPROXIMATION

The equations approximating the steady-state current between any two electrodes (or arbitrary shape) forming a thin layer cell can be derived in all cases by modelling each electrode as a series of contiguous, thin circular strips, each of which approximates a parallel-plate electrode of equivalent area (see Fig. 2b). The fluxes of electroactive species to and from these strips are furthermore assumed to be parallel to the axis of symmetry passing through both electrodes (e.g., for the hemispherical cell, the line passing through the hemispheres' centers). This approximation implies that each strip of one electrode "communicates" electrochemically with only the corresponding strip on the other electrode. The current generated by the thin layer cell is then approximated by summing the individual currents generated by the series of parallel-plate electrodes.

The fundamental equation on which these derivations rest relates the steady-state diffusion-limited current Δi between two parallel-plate electrodes of area ΔA separated by the distance l to the concentrations and diffusion coefficients of all electroactive species. The analysis is simplified if only the oxidized (Ox) and reduced (Red) forms of one species are present each at a bulk concentration c^* and the two species have equal diffusion coefficients, D. If the electrodes are perpendicular to the axis of symmetry z, then at steady state

$$D\frac{d^2c_O}{dz^2} = D\frac{d^2c_R}{dz^2} = 0 \tag{1}$$

and

$$\Delta i = 2nF\,\Delta A Dc^*/l \tag{2}$$

where nF is the charge passed during 1 mol of reaction and c_O and c_R are the concentrations of the oxidized and reduced forms of the couple, which depend on z.

Twin hemispherical electrodes

The steady-state currents at a number of electrode pairs of different geometry can be derived, using eqn. (2) as a starting basis. For two hemispheres of radius R separated by the distance r_0, the span l between any two parallel strips is (see Fig. 2b)

$$l = r_0 + 2h \tag{3a}$$

where

$$h = R(1 - \cos\theta) \tag{3b}$$

The angle θ is measured with respect to the axial symmetry axis, as shown in the figure, and the area ΔA of each strip is $2\pi R^2 \sin\theta\,\Delta\theta$. The magnitude Δi of current at each strip is thus

$$\Delta i = \frac{4\pi R^2 nFDc^* \sin\theta\,\Delta\theta}{r_0 + 2R(1 - \cos\theta)} \tag{4}$$

or, in (dimensionless) differential form

$$\frac{\mathrm{d}i}{2\pi RnFDc^*} = \frac{2\sin\theta\,\mathrm{d}\theta}{\gamma + 2(1 - \cos\theta)} = \frac{\partial f}{\partial n}\sin\theta\,\mathrm{d}\theta \equiv \mathrm{d}I_1 \tag{5}$$

where $\gamma = r_0/R$, $\partial f/\partial n$ is the dimensionless concentration gradient at the electrode surface, and I_1 is the dimensionless steady-state current.

The expression for I_1 is obtained by summing over all of the $\mathrm{d}i$ contributions, i.e., by integrating the second term in eqn. (5) over all appropriate θ values

$$I_1 = \frac{i}{2\pi RnFDc^*} = 2\int_0^{\pi/2} \frac{\sin\theta\,\mathrm{d}\theta}{\gamma + 2(1 - \cos\theta)} = \ln(1 + 2/\gamma) \tag{6}$$

Note that, in contrast to the parallel-plate electrode for which the current is inversely proportional to the separation distance, I_1 increases only as the logarithm of the separation distance. At very short distances, when $\gamma \ll 1$, $I_1 \approx \ln(2R/r_0)$.

Hemisphere-plane electrodes

If the cell is formed from a single hemispherical electrode of radius R facing a planar electrode, and the two are separated by the distance r_0, as shown in Fig. 2c, the dimensionless current I_1 is

$$I_1 = \frac{i}{2\pi RnFDc^*} = \ln(1 + \gamma^{-1}) \tag{7a}$$

$$I_1 \approx \ln(R/r_0) \qquad \gamma \ll 1 \tag{7b}$$

where $\gamma = r_0/R$ as before.

Twin conical electrodes

For a cell formed from two right circular cone electrodes separated by r_0 and facing one another as shown in Fig. 2d, the dimensionless current I_1 is similarly derived. The area ΔA of the thin circular strip in this case can be shown to equal $2\pi r(1+\alpha^2)^{1/2}\Delta r/\alpha$, where r is the strip radius and α, the aspect ratio, equals the radius R' of the conical base divided by the conical height H. Equation (2) becomes

$$\Delta i = \frac{4\pi(1+\alpha^2)^{1/2} nFDc^* r\,\Delta r}{\alpha(r_0 + 2r/\alpha)} \tag{8}$$

where $l = r_0 + 2r/\alpha$ is the span between the corresponding electrode strips. Writing eqn. (8) in its differential form and integrating from $r = 0$ to $r = R'$, one obtains after some algebraic manuipulation

$$I_1 = \frac{i}{2\pi R' nFDc^*} = (1+\alpha^2)^{1/2}\left(\frac{1}{2} - \frac{\gamma'}{4}\ln(1 + 2/\gamma')\right) \tag{9}$$

where $\gamma' = r_0/H$.

Cone / plane electrodes

For a right circular cone and a planar electrode separated by r_0 (see Fig. 2e), the current I_1 is

$$I_1 = \frac{i}{2\pi R' nFDc^*} = (1+\alpha^2)^{1/2}(1 - \gamma' \ln(1 + 1/\gamma')) \tag{10}$$

Crossed-cylinder electrodes

For completeness we include the formula for the steady-state current at crossed-cylinder electrodes (see Fig. 1), based on the one-dimensional-flux approximation and derived elsewhere [2]:

$$I_1 = \frac{ih_0}{2\pi a_0 b_0 nFDc^*} = 1 - \gamma^* \ln(1 + 1/\gamma^*) \tag{11}$$

Here a_0 and b_0 are the major and minor axes of the ellipse defining the effective electrode area, $h_0 = (a_0^2 - b_0^2)^{1/2}$, $\gamma^* = r_0/h_0$, and r_0 is again the separation distance between the electrodes.

Interestingly, eqns. (9)–(11) predict that the currents generated by these last three cells are independent of the separation distance as $\gamma \to 0$, in agreement with experiments based on the crossed-cylinder cell [2]. These various I_1's are plotted as functions of the various γ's in Fig. 3.

COMPLETE FORMULATION OF THE TWIN-HEMISPHERICAL-ELECTRODE PROBLEM

To test the accuracy of the approximation for the steady-state currents in the different thin layer cells, which neglects lateral diffusion between the cylindrical

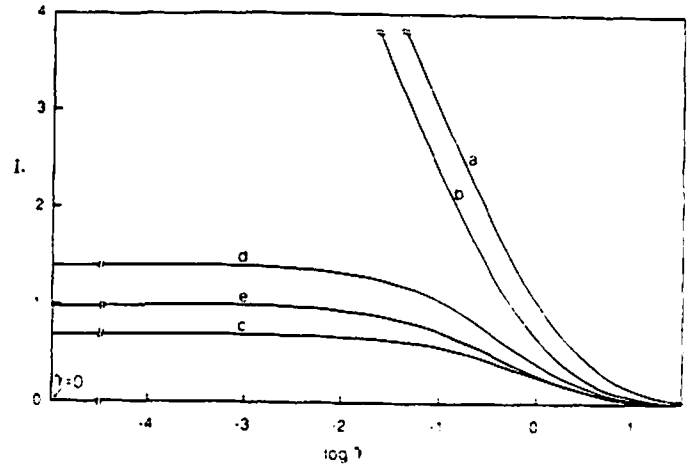

Fig. 3. Steady-state current I_1 vs. γ for the (a) twin hemispherical cell, (b) hemisphere/plane cell, (c) twin conical cell, (d) cone/plane cell, and (e) crossed-cylinder cell. $\alpha = 1$.

solution elements and from outside the interelectrode gap, a more complete analysis of the diffusion-limited current generated in the twin hemispherical cell was undertaken. The full treatment also allows a determination of the time required, from the initial imposition of potential between the electrodes, for the current to attain its steady-state value. In general, for any thin layer cell, the consideration of additional fluxes orthogonal to the axial flux treated above necessitates solving the continuity equations for the concentration profiles of all electroactive species and calculating from these profiles all fluxes to the electrodes. For the radially symmetric hemispherical cell examined in detail here, the continuity equation is best expressed in cylindrical polar coordinates. If the oxidized and reduced forms of only one species are present, then

$$\frac{\partial c_O}{\partial t} = D_O\left(\frac{\partial^2 c_O}{\partial r^2} + \frac{1}{r}\frac{\partial c_O}{\partial r} + \frac{\partial^2 c_O}{\partial z^2}\right) \tag{12}$$

$$\frac{\partial c_R}{\partial t} = D_R\left(\frac{\partial^2 c_R}{\partial r^2} + \frac{1}{r}\frac{\partial c_R}{\partial r} + \frac{\partial^2 c_R}{\partial z^2}\right) \tag{13}$$

where c_O (c_R) and D_O (D_R) are the concentration and diffusion coefficient of the oxidized (reduced) form, t is time, and r and z are the radial and axial coordinates defined in Fig. 2b. No angular flux appears in the equations because of radial symmetry. Hence the three-dimensional transport problem is effectively a two-dimensional one, which requires solutions for c_O and c_R in a plane passing through the centers of the two hemispheres (see Figs. 4a and 4b).

If Ox, initially present at concentration c_O^*, is exhaustively reduced at the upper hemisphere, and Red, initially present at concentration c_R^*, is exhaustively oxidized

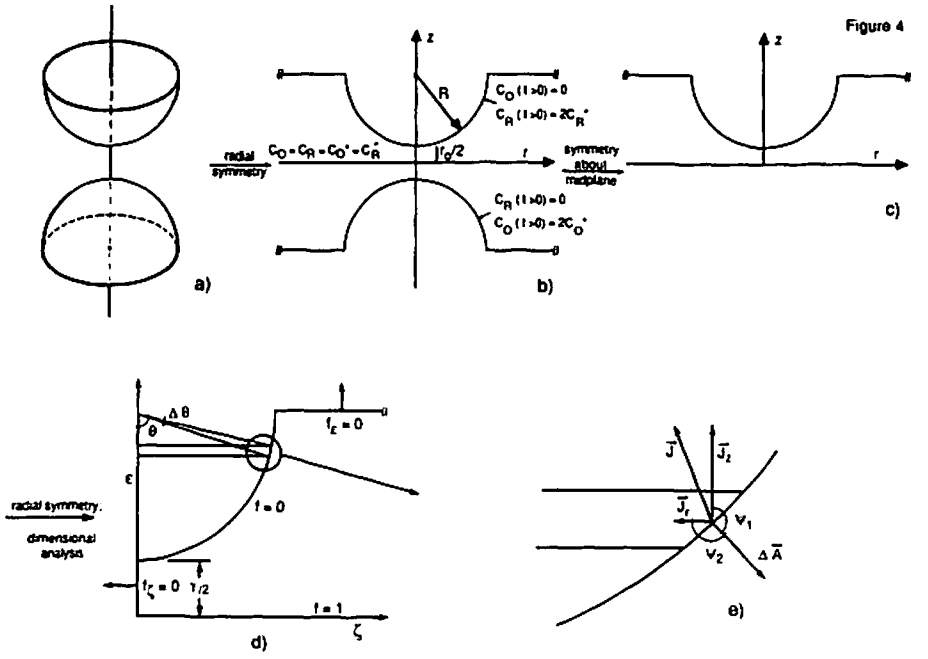

Fig. 4. Simplification of current calculation by use of symmetry. (a, b) Reduction from three to two dimensions by radial symmetry. Shaded areas represent non-conducting planes. (b, c) Replacement of eqn. (18) by eqn. (20) as a boundary condition. (c, d) Reduction from two quadrants to one quadrant by radial symmetry. (d) Schematic representation of boundary conditions. (e) Vector representation of two-dimensional flux to electrode surface.

at the lower hemisphere, the initial and boundary conditions that must be satisfied are

$$c_O(\Phi,\ t=0) = c_O^* \tag{14}$$

$$c_R(\Phi,\ t=0) = c_R^* \tag{15}$$

$$c_O(\Phi_1,\ t>0) = 0 \tag{16}$$

$$c_R(\Phi_2,\ t>0) = 0 \tag{17}$$

$$\int_{\Phi_1,\Phi_2}\left(\left(D_R\frac{\partial c_R}{\partial r} + D_O\frac{\partial c_O}{\partial r}\right)\vec{r} + \left(D_R\frac{\partial c_R}{\partial z} + D_O\frac{\partial c_O}{\partial z}\right)\vec{z}\right)\cdot\overrightarrow{dA} = 0 \tag{18}$$

where Φ, Φ_1, and Φ_2 are functions of r and z describing the physical volume occupied by solution and the surface areas of the upper and lower hemispheres, respectively, $\vec{r}$ and $\vec{z}$ are unit vectors in the r and z directions, and $\overrightarrow{dA}$ is a vector representing any differential area element of either hemisphere. The final equation states that the flux of Ox to the upper and Red to the lower electrode must equal the flux of Red away from the upper and Ox away from the lower electrode.

The solution of this problem is greatly simplified if a limiting case is considered, in which $c_O^* = c_R^* = c^*$ and $D_O = D_R = D$. For this case, these equations imply that at the electrode surfaces

$$c_R(\Phi_1,\ t>0) = c_O(\Phi_2,\ t>0) = 2c_O^* = 2c_R^* = 2c^* \tag{19}$$

In light of eqns. (16) and (17), a plane must exist between the hemispheres at $z = 0$ at which

$$c_O = c_R = c_O^* = c_R^* = c^*, \qquad z = 0 \tag{20}$$

at all times (see Fig. 4b). Because concentrations in this plane do not change with time, eqn. (20) can replace eqn. (18) as a boundary condition, and solutions for c_O and c_R are consequently required only in the upper half of the r–z plane (see Fig. 4b and 4c). Furthermore, since $c_O(r,\ z) = c_O(-r,\ z)$ and $c_R(r,\ z) = c_R(-r,\ z)$ because of radial symmetry, the problem is again simplified and solutions to eqns. (12) and (13) are subsequently required only in the first quadrant of the r–z plane (see Figs. 4c and 4d). In addition, reflection of the Ox concentration profile in the $z = 0$ midplane yields the Red profile at all times, and only one (e.g., eqn. 12) of the continuity equations must be solved. Finally, to simplify the problem further, it is assumed that both hemispherical electrodes are affixed to non-conducting infinite planes, which confine the solution such that $|z| \leqslant r_0/2 + R$, as shown in Figs. 4a–4d.

Equations (12) is cast here in a dimensionless form prior to finding its solution. Introducing the variables

$$\zeta = r/R \tag{21}$$

$$\epsilon = z/R \tag{22}$$

$$f = c_O/c_O^* = c_O/c^* \tag{23}$$

$$T = D_O t/R^2 = Dt/R^2 \tag{24}$$

eqn. (12) can be written as

$$\frac{\partial f}{\partial T} = \frac{\partial^2 f}{\partial \zeta^2} + \frac{1}{\zeta}\frac{\partial f}{\partial \zeta} + \frac{\partial^2 f}{\partial \epsilon^2} = f_{\zeta\zeta} + \frac{1}{\zeta} f_\zeta + f_{\epsilon\epsilon} \tag{25}$$

subject to the initial and boundary conditions

$$f(\Phi',\ T=0) = 1 \tag{26}$$

$$f(\Phi_1',\ T>0) = 0 \tag{27}$$

$$f(\epsilon=0,\ T\geqslant 0) = 1 \tag{28}$$

where Φ' and Φ_1' are the equivalent solution volume and surface area described above, but now expressed in dimensionless units, and the subscripts on f denote differentiation with respect to the subscript variable. The expressions for Φ' and Φ_1' are, respectively

$$\Phi'\colon \zeta > \left(1 - (\epsilon - (1+\gamma/2))^2\right)^{1/2}, \qquad \gamma/2 \leqslant \epsilon \leqslant 1+\gamma/2;\ \zeta \geqslant 0,\ 0 \leqslant \epsilon < \gamma/2 \tag{29}$$

$$\Phi_1'\colon \zeta = \left(1 - (\epsilon - (1+\gamma/2))^2\right)^{1/2}, \qquad \gamma/2 \leqslant \epsilon \leqslant 1+\gamma/2 \tag{30}$$

where, as before, $\gamma = r_0/R$, the dimensionless separation distance between the hemispheres.

Since eqn. (25) is second order in ζ and ϵ and first order in T, one initial and four boundary conditions must be specified. Two additional boundary conditions are

$$f_\zeta|_{\zeta=0} = 0, \qquad 0 \leqslant \epsilon < \gamma/2 \tag{31}$$

$$f_\epsilon|_{\epsilon=1+\gamma/2} = 0, \qquad \zeta > 1 \tag{32}$$

The first is a consequence of radial symmetry. The second implies that Ox does not cross the plane to which the upper hemisphere is affixed. All four boundary conditions are represented schematically in Fig. 4d.

The current generated by the cell is calculated from Fick's first law. The charge in mol/s crossing the small area band $\overrightarrow{\Delta A}$ shown in Fig. 4d is given by the dot product

$$\vec{J}\cdot\overrightarrow{\Delta A} \tag{33}$$

where $\vec{J} = \vec{J}_r + \vec{J}_z$ is the vector sum of flux in the radial ($\vec{J}_r$) and axial ($\vec{J}_z$) directions and the vector $\overrightarrow{\Delta A}$ has the magnitude $|\overrightarrow{\Delta A}|$ and a direction normal to the surface. Thus the (signed) current Δi at arena $\overrightarrow{\Delta A}$ is

$$\Delta i = nF\vec{J}\cdot\overrightarrow{\Delta A} \tag{34}$$

Since

$$\vec{J}_r = -D_O\frac{\partial c_O}{\partial r}\vec{r} \tag{35}$$

$$\vec{J}_z = -D_O\frac{\partial c_O}{\partial z}\vec{z} \tag{36}$$

and the magnitude $|\overrightarrow{\Delta A}|$ of the area strip in Fig. 4d is

$$|\overrightarrow{\Delta A}| = 2\pi R^2 \sin\theta\,\Delta\theta \tag{37}$$

Δi for this strip equals

$$\Delta i = -nFD_O\left(\left(\frac{\partial c_O}{\partial r}\right)_s\vec{r} + \left(\frac{\partial c_O}{\partial z}\right)_s\vec{z}\right)\cdot\overrightarrow{\Delta A} \tag{38}$$

or

$$\Delta i = -2\pi R^2 nFD_O\left(\left|\frac{\partial c_O}{\partial r}\right|_s\cos\Psi_2 + \left|\frac{\partial c_O}{\partial z}\right|_s\cos\Psi_1\right)\sin\theta\,\Delta\theta \tag{39}$$

where the angles Ψ_1 and Ψ_2 are defined in Fig. 4e and the subscript "s" denotes evaluation of the derivatives at the electrode surface. (The vertical bars indicate absolute values, i.e., $|x| = |-x|$.) Expressing Ψ_1 and Ψ_2 in terms of θ and using eqns. (21)–(23), eqn. (39) can be rewritten in dimensionless form as

$$\frac{\Delta i}{2\pi RnFDc^*} = -\left(\left|\frac{\partial f}{\partial\zeta}\right|_s\sin^2\theta + \left|\frac{\partial f}{\partial\epsilon}\right|_s\sin 2\theta/2\right)\Delta\theta \tag{40}$$

or, in differential form, as

$$\frac{di}{2\pi RnFDc^*} = -\left(\left|\frac{\partial f}{\partial \zeta}\right|_s \sin^2\theta + \left|\frac{\partial f}{\partial \epsilon}\right|_s \sin 2\theta/2\right) d\theta = \frac{\partial f}{\partial n}\sin\theta\, d\theta \equiv -dI_2 \qquad (41)$$

where $\partial f/\partial n$ is the dimensionless concentration gradient (cf. eqn. 5) normal to the electrode surface. As before, the magnitude I_2 of the dimensionless current is obtained by integrating the second term in eqn. (41) from $\theta = 0$ to $\theta = \pi/2$

$$I_2 = \frac{|i|}{2\pi RnFDc^*} = \int_0^{\pi/2}\left(\left|\frac{\partial f}{\partial \zeta}\right|_s \sin^2\theta + \left|\frac{\partial f}{\partial \epsilon}\right|_s \sin 2\theta/2\right) d\theta \qquad (42)$$

The current I_2 is defined by the absolute value of i, which is negative because the angle between $\vec{J}$ and $\overrightarrow{dA}$ lies between $\pi/2$ and π.

The current I_2 is always greater than or equal to I_1 for all γ, as is now argued. If the sum $f_{\zeta\zeta} + f_\zeta/\zeta$ were zero for all ζ and ϵ, eqn. (25) would reduce to the one-dimensional diffusion equation from which I_1 was derived. In this case $\partial f/\partial T < 0$ and thus $f_{\epsilon\epsilon} \leqslant 0$ at the electrode surface, equalling zero only under steady-state conditions. The sum $f_{\zeta\zeta} + f_\zeta/\zeta$ is not zero at the electrode surface, however, but is less than or equal to zero, because Ox diffuses to the upper hemisphere from the surrounding solution. The right-hand side of eqn. (25) is consequently always $\leqslant f_{\epsilon\epsilon}$. Since the current increases as $\partial f/\partial T$ decreases (i.e., increases in absolute value), $I_2 \geqslant I_1$.

Since I_2 depends on $\partial f/\partial \zeta|_s$ and $\partial f/\partial \epsilon|_s$, eqn. (25) must be solved for f prior to the computation of I_2. Both f and I_2 were determined numerically, as described below.

NUMERICAL ANALYSIS

Equation (25) was solved numerically using finite difference equations that approximate the spatial and temporal derivatives of f at discrete points in the ζ–ϵ plane by algebraic equations. Approximating the temporal derivative at the arbitrary point $f = f_0$ ($\zeta = \zeta_0$, $\epsilon = \epsilon_0$) by

$$\frac{\partial f}{\partial T} = \frac{f_{T+\Delta T} - f_T}{\Delta T} \qquad (43)$$

where $\Delta T = \Delta(Dt/R^2) = D\,\Delta t/R^2$, eqn. (25) can be approximated as

$$f_{T+\Delta T} = f_T + \Delta T\left(f_{\zeta\zeta} + \frac{1}{\zeta} f_\zeta + f_{\epsilon\epsilon}\right) \qquad (44)$$

Thus f at any time $T + \Delta T$ can be calculated at the point $f_0 = f_0(\zeta_0, \epsilon_0)$ from knowledge of f_0 and the spatial derivatives of f at f_0 and time T. Since $f(\Phi', T = 0) = 1$, f's at subsequent times can be calculated iteratively.

Two types of two-dimensional networks (i.e., sets of discrete points (ζ_0, ϵ_0)) were used to compute f and its derivatives. The first is the modified square network shown in Fig. 5a in which all points well removed from the circular boundary were

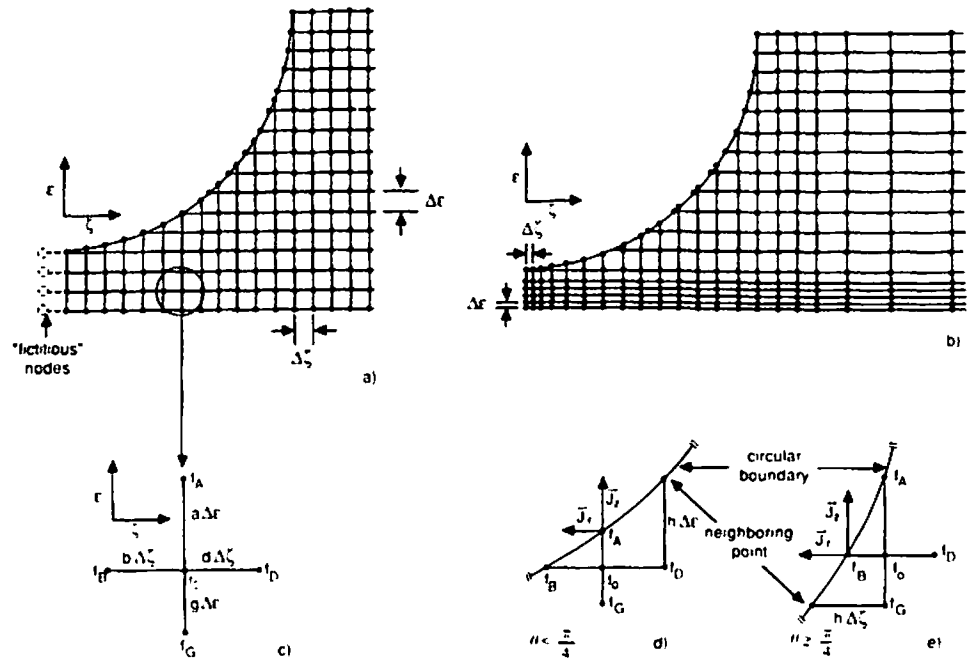

Fig. 5. Two-dimensional networks used in solving eqn. (25) numerically. (a) Square network. Note "ficticious" nodes f_B at $\zeta = -\Delta\zeta$. (b) Exponential network. (c) Five-star network from which spatial derivatives were calculated. (d, e) Networks from which surface derivatives were calculated.

separated from their four nearest neighbors in the ζ and ϵ directions by the dimensionless spacing $\Delta\zeta = \Delta\epsilon$. Points nearest the circular boundary were separated from their neighbors on the boundary by irregular spacings slightly greater than $\Delta\zeta$. The second network, which is computationally more efficient than the first (especially for small γ), consists of a central square network (as described above) that connects a network expanding exponentially away from the circular boundary to one that collapses exponentially near the origin (see Fig. 5b). In these exponential networks, the distances between any three colinear points are such that the second is a constant multiple of the first. By use of these combined subnetworks, the total network is kept relatively small, even for small γ. The smallest spacing between points, at the base of the collapsing exponential network, is $\Delta\zeta = \Delta\epsilon$.

These exponential networks should not be confused with those introduced by Joslin and Pletcher [5] and refined by Feldberg [6]. In their networks, the rectangular cells formed by intersecting nodal lines are associated with representative concentrations located near (but not at) the centers of the rectangles. Here, the points f_0 represent concentrations at the intersections of the nodal lines.

Numerical approximations to the spatial derivatives f_ζ, $f_{\zeta\zeta}$, and $f_{\epsilon\epsilon}$ at each f_0 were calculated from finite difference equations derived from the irregular five-star network connecting f_0 with its four nearest neighbors in the ϵ and ζ directions, as

shown in Fig. 5c. These neighboring concentrations f_A, f_B, f_D, and f_G (which can represent either boundary values or solution concentrations) were expressed as truncated Taylor series expansions around f_0 [7–9], viz.

$$f_A = f_0 + a\,\Delta\epsilon f_\epsilon + a^2\,\Delta\epsilon^2 f_{\epsilon\epsilon}/2 + \cdots \tag{45}$$

$$f_B = f_0 - b\,\Delta\zeta f_\zeta + b^2\,\Delta\zeta^2 f_{\zeta\zeta}/2 + \cdots \tag{46}$$

$$f_D = f_0 + d\,\Delta\zeta f_\zeta + d^2\,\Delta\zeta^2 f_{\zeta\zeta}/2 + \cdots \tag{47}$$

$$f_G = f_0 - g\,\Delta\epsilon f_\epsilon + g^2\,\Delta\epsilon^2 f_{\epsilon\epsilon}/2 + \cdots \tag{48}$$

where $a\,\Delta\epsilon$, $b\,\Delta\zeta$, $d\,\Delta\zeta$, and $g\,\Delta\epsilon$ are the dimensionless distances between f_0 and the adjacent network element and f_ζ, f_ϵ, $f_{\zeta\zeta}$, and $f_{\epsilon\epsilon}$ are the first and second derivatives of f at f_0 at time T. These equations are combined to obtain the following spatial derivatives

$$f_\zeta = \frac{1}{\Delta\zeta}\frac{f_D - (d/b)^2 f_B - \left(1-(d/b)^2\right) f_0}{d + d^2/b} + O(\Delta\zeta^2) \tag{49}$$

$$\left.\begin{aligned} \frac{1}{\zeta} f_\zeta &= \frac{1}{X\,\Delta\zeta^2}\frac{f_D - (d/b)^2 f_B - \left(1-(d/b)^2\right) f_0}{d + d^2/b} + O(\Delta\zeta) \\ &\equiv \frac{1}{X\,\Delta\zeta^2} F(f_B, f_D, f_0, b, d) + O(\Delta\zeta) \end{aligned}\right\} \tag{50}$$

$$\left.\begin{aligned} f_{\zeta\zeta} &= \frac{2}{\Delta\zeta^2}\frac{f_D + d f_B/b - (1 + d/b) f_0}{bd + d^2} + O(\Delta\zeta) \\ &\equiv \frac{2}{\Delta\zeta^2} G(f_B, f_D, f_0, b, d) + O(\Delta\zeta) \end{aligned}\right\} \tag{51}$$

$$\left.\begin{aligned} f_{\epsilon\epsilon} &= \frac{2}{\Delta\epsilon^2}\frac{f_A + a f_G/g - (1 + a/g) f_0}{ag + a^2} + O(\Delta\epsilon) \\ &\equiv \frac{2}{\Delta\epsilon^2} H(f_A, f_G, f_0, a, g) + O(\Delta\epsilon) \end{aligned}\right\} \tag{52}$$

where $O(\beta)$ is a truncation error of order β, $X = \zeta/\Delta\zeta$, and the functions F, G, and H are defined by the 3-term difference equations.

From these equations, algebraic approximations to eqn. (25) were derived for all f_0's. In particular, the approximation for all f_0's within the boundaries shown in Figs. 5a and 5b was obtained by substituting eqns. (50)–(52) into eqn. (44) and equating $\Delta\zeta$ to $\Delta\epsilon$

$$f_{T+\Delta T} = f_T + \frac{\Delta T}{\Delta\zeta^2}(2G + F/X + 2H) + O(\Delta\zeta) \qquad \text{for all } \Phi' \tag{53}$$

Here $\Delta T/\Delta\zeta^2 = D\,\Delta t/R^2\,\Delta\zeta^2 \equiv$ DMA is a dimensionless time whose magnitude determines the time interval between successive iterations. Its upper limit is dictated by the requirement that f remain non-negative and consequently depends on the magnitudes of the scaling coefficients a, b, d, and g. When these coefficients are $\geqslant 1$ (i.e., when $\Delta\zeta$ and $\Delta\epsilon$ are the minimum spacings between adjacent points), the upper limit to DMA can be shown to equal 2/9, which is somewhat smaller than the maximum DMA associated with one- and two-dimensional rectangular networks, DMA = 1/2 and 1/4, respectively. (The small difference is attributable to the term f_ζ/ζ.) The stability of all calculations reported here was assured by choosing DMA $\leqslant 0.22$.

The boundary condition, eqn. (31), was implemented by equating the "ficticious" node f_B to f_D for all f_0 at $\zeta = 0$, as required by radial symmetry (see Fig. 5a). The singularity in the term f_ζ/ζ at $\zeta = 0$ was addressed by L'Hospital's rule [9]. The result, obtained by differentiating both numerator and denominator with respect to ζ and taking the $\zeta \to 0$ limit, is

$$\lim_{\zeta\to 0} f_\zeta/\zeta = f_{\zeta\zeta} \tag{54}$$

and thus

$$f_{T+\Delta T} = f_T + \mathrm{DMA}(4G + 2H) + O(\Delta\zeta) \qquad \zeta = 0,\ 0 \leqslant \epsilon < \gamma/2 \tag{55}$$

with $f_B = f_D$ in expression G for all $\zeta = 0$.

The boundary condition, eqn. (32), cannot be implemented as above because no nodal element f_A exists above the planar boundary. Equation (48) was rearranged instead to give, with $f_\epsilon = 0$

$$f_{\epsilon\epsilon} = \frac{2}{g^2\,\Delta\epsilon^2}(f_G - f_0) + O(\Delta\epsilon), \qquad \epsilon = 1 + \gamma/2,\ \zeta > 1 \tag{56}$$

and eqn. (44) for this case we approximated as

$$f_{T+\Delta T} = f_T + \mathrm{DMA}\big(2G + F/X + 2(f_G - f_0)/g^2\big) + O(\Delta\epsilon), \qquad \epsilon = 1 + \gamma/2,\ \zeta > 1 \tag{57}$$

The derivatives $\partial f/\partial\zeta|_s$ and $\partial f/\partial\epsilon|_s$ required to calculate current I_2 were estimated at discrete θ values by fitting the f_A, f_B, f_D, and f_G values comprising each five-star network adjacent to the circular boundary, and one additional neighboring point on the boundary (see Figs. 5d and 5e), to the following truncated Taylor series expansion about f_0 [10]

$$f = f_0 + f_\zeta(\zeta - \zeta_0) + f_\epsilon(\epsilon - \epsilon_0) + \tfrac{1}{2}f_{\zeta\zeta}(\zeta - \zeta_0)^2 + \tfrac{1}{2}f_{\epsilon\epsilon}(\epsilon - \epsilon_0)^2 + f_{\zeta\epsilon}(\zeta - \zeta_0)(\epsilon - \epsilon_0) + \cdots \tag{58}$$

The cross derivative $f_{\zeta\epsilon}$ at f_0 equals approximately

$$f_{\zeta\epsilon} = -\frac{f_0 + f_\zeta d\,\Delta\zeta + f_\epsilon h\,\Delta\epsilon + f_{\zeta\zeta}(d\,\Delta\zeta)^2/2 + f_{\epsilon\epsilon}(h\,\Delta\epsilon)^2/2}{dh\,\Delta\zeta\,\Delta\epsilon} + O(\Delta\zeta) \tag{59}$$

when the five points fit to eqn. (58) are spatially oriented as in Fig. 5d. (Quantity h is defined in the figure.) Differentiating this equation with respect to ζ and ϵ and evaluating the derivatives at f_A (i.e., on the circular boundary representing the electrode surface), one obtains

$$\left.\frac{\partial f}{\partial \zeta}\right|_s = f_\zeta + f_{\zeta\epsilon} a\ \Delta\epsilon + O(\Delta\epsilon^2) \tag{60}$$

$$\left.\frac{\partial f}{\partial \epsilon}\right|_s = f_\epsilon + f_{\epsilon\epsilon} a\ \Delta\epsilon + O(\Delta\epsilon^2) \tag{61}$$

Such fits to eqn. (58) were made only when $\theta < \pi/4$. For $\pi/4 \leqslant \theta \leqslant \pi/2$, the five points fit to eqn. (58) were spatially oriented as in Fig. 5e. For these cases, eqns. (59)–(61) are replaced by

$$f_{\zeta\epsilon} = \frac{f_\zeta h\ \Delta\zeta + f_\epsilon g\ \Delta\epsilon - \left(f_0 + f_{\zeta\zeta}(h\ \Delta\zeta)^2/2 + f_{\epsilon\epsilon}(g\ \Delta\epsilon)^2/2\right)}{gh\ \Delta\epsilon\ \Delta\zeta} + O(\Delta\zeta) \tag{62}$$

$$\left.\frac{\partial f}{\partial \zeta}\right|_s = f_\zeta - f_{\zeta\zeta} b\ \Delta\zeta + O(\Delta\zeta^2) \tag{63}$$

$$\left.\frac{\partial f}{\partial \epsilon}\right|_s = f_\epsilon - f_{\zeta\epsilon} b\ \Delta\zeta + O(\Delta\zeta^2) \tag{64}$$

Note that the expressions for the surface derivatives are more accurate than the other spatial derivatives. The high accuracy of the surface derivatives is a prerequisite to calculating accurate currents.

The dimensionless current I_2 was then calculated from these surface derivatives and eqn. (42). The integral was computed using Simpson's rule, as modified for an irregularly spaced net of θ values.

The validity of this numerical formulation was affirmed by material balance [11]. As long as the diffusion layers formed at the hemispheres do not overlap, the charge passed at the electrodes corresponds directly to the depletion of electroactive species in the immediate electrode vicinity. At the upper electrode, for example, where Ox is reduced to Red

$$\int_0^t i\ \mathrm{d}t' = nF \int_\Phi (c_O^* - c_O)\ \mathrm{d}V \tag{65}$$

where $\mathrm{d}V = 2\pi r\ \mathrm{d}r\ \mathrm{d}z$ is the differential cylindrical volume element and the volume Φ over which integration occurs is sufficiently large to include all $c_O < c_O^*$. With the dimensionless parameters defined above, eqn. (65) can also be written as

$$\int_0^T I_2\ \mathrm{d}T' = \int_{\Phi'} (1 - f)\zeta\ \mathrm{d}\zeta\ \mathrm{d}\epsilon \tag{66}$$

The numerical evaluation of both of these integrals yields results differing by only a percent or so, even after thousands of iterations, thus confirming the method.

All calculations were carred out on a CRAY X-MP/24 supercomputer at the Balcones Research Center of the University of Texas.

RESULTS AND DISCUSSION

Figure 6 is a plot of current I_2 vs. time T for various separation distances γ. The bottom six and top two solid curves were generated using the square and exponential networks, respectively; the I_2 corresponding to the separation $\gamma = 0.009983$ was determined using both networks. In this case, the exponential-network computation (represented by the dashed curve) required only one-fiftieth of the time required by the square-network calculation (represented by the solid curve). The latter calculation was stopped slightly prior to reaching quasi-steady state because of this inefficiency. The discretization error between these curves, approximately 2.2%, is quite small.

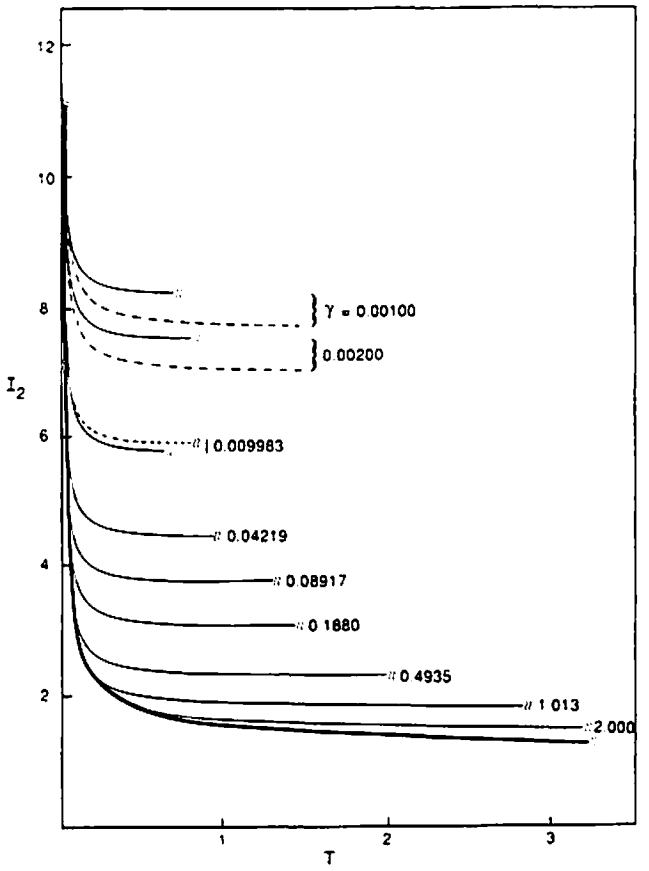

Fig. 6. Instantaneous current I_2 vs. time T for various γ. Solid curves were calculated numerically; bottom boldface curve was calculated from eqn. (68). Upper two dashed curves represent analytical approximations given by eqn. (72). $T = Dt/R^2$; $\gamma = r_0/R$.

An analytical limit, which the numerical results must satisfy, exists for I_2 as $\gamma \to \infty$. In this case, the time at which the two electrodes' diffusion layers overlap approaches infinity. Prior to this time (i.e., for any finite T), the diffusion layer at each electrode is hemispherical and the surface concentration gradient is uniform over the whole electrode surface, as will be shown below. The hemispherical diffusion-limited current $i_{2\infty}$ for this case should consequently equal 1/2 the diffusion-limited current i_d at a spherical electrode of radius R, which is [12]

$$2i_{2\infty} = i_d = 4\pi R^2 nFDc^* \left(\frac{1}{(\pi Dt)^{1/2}} + \frac{1}{R} \right) \tag{67}$$

The factor 1/2 is introduced because the surface area of a hemisphere is one-half that of a sphere. Using eqn. (24), eqn. (67) can be written in the dimensionless form

$$\frac{i_{2\infty}}{2\pi RnFDc^*} = \frac{1}{(\pi T)^{1/2}} + 1 = \left| \frac{\partial f}{\partial n} \right| \equiv I_{2\infty} \tag{68}$$

where, as before, $\partial f/\partial n$ is the dimensionless normal derivative at the electrode surface and $I_{2\infty}$ is the dimensionless limiting current. The bottom bold curve in Fig. 6 is a graph of eqn. (68). A short times the numerical calculations superimpose on this curve, as expected. The time at which the results diverge from eqn. (68) also decreases as γ decreases, since feedback becomes increasingly significant at short T for small γ.

The current I_1 clearly differs from the numerical evaluations of I_2 when $\gamma > 1$; eqn. (6) predicts that $I_1 \to 0$ and the numerical results, in conjunction with eqn. (68), suggest that $I_2 \to 1$, as T and γ approach infinity. The discrepancy decreases significantly, however, as γ is reduced. Table 1 reports the absolute and relative errors between I_1 and the limiting I_2 value, as determined from Fig. 6, for various γ. (Not all of these I_2's are plotted in Fig. 6.) The relative error is already less than ~ 0.1 for $\gamma < 0.01$. The absolute error $I_2 - I_1$ is interestingly constant, equalling 0.602 ± 0.006, over the 42-fold range, $0.001 \leqslant \gamma \leqslant 0.04219$. Since $I_2 \geqslant I_1$ on theoretical grounds for all γ, eqn. (6) approximates the quasi-steady state I_2 value to within 10%, as long as $\gamma < 0.01$.

Because the solution volume is unbounded in the ζ direction, $\partial f/\partial T \leqslant 0$ for all f and the concentration profile never reaches steady state. As shown in Fig. 6, the current I_2 nevertheless approaches a steady-state value, implying that $\partial f/\partial T \approx 0$ in the immediate vicinity of the electrode. This steady-state current can be calculated directly by equating $\partial f/\partial T$ in eqn. (25) to zero. Such a calculation sacrifices a description of the current transient but is independent of ΔT, which must be excessively small when $\gamma \ll 1$ and $\Delta\zeta \ll 1$. (As a consequence, $\sim 5 \times 10^7$ iterations were required to generate the uppermost curve in Fig. 6.) The steady-state calculation was implemented by setting equal to zero the expressions in the parentheses of eqns. (53), (55), and (57), solving these expressions for f_0 in terms of f_A, f_B, f_D, and f_G, guessing the initial values of all f_0's, and calculating iteratively new f_0's from previous ones, until I_2 converged to a nearly constant value. Only a few thousand

TABLE 1
Absolute and relative errors between I_1 and I_2 values determined from Fig. 6. I_1 was computed from eqn. (6)

γ	I_1	I_2 (T)	$(I_2 - I_1)/I_2$	$I_2 - I_1$
0.00100	7.601	8.208 (0.688)	0.0740	0.607
0.00200	6.909	7.503 (0.810)	0.0792	0.594
0.009983	5.305	5.904 (0.792) [a]	0.101	0.599
0.04219	3.879	4.485 (0.923)	0.135	0.606
0.08917	3.154	3.775 (1.298)	0.165	0.621
0.1880	2.454	3.109 (1.438)	0.211	0.655
0.3284 [b]	1.959	2.646 (1.871)	0.260	0.687
0.4935	1.620	2.338 (2.010)	0.307	0.718
0.7463 [b]	1.303	2.055 (2.553)	0.366	0.752
1.013	1.090	1.869 (2.833)	0.417	0.779
1.522 [b]	0.839	1.655 (3.916)	0.493	0.816
2.000	0.693	1.534 (4.825) [c]	0.548	0.841

[a] Based on exponential-network calculation.
[b] Curve not shown in Fig. 6.
[c] Complete transient not shown in Fig. 6.

iterations were required to reach steady state using this procedure, irrespective of γ. Table 2 reports the relative and absolute errors between I_1 and the steady-state I_2 computed as described here. Note that the I_2's for $\gamma = 0.001$ and 0.002 are only slightly smaller than the corresponding values reported in Table 1. As observed above, the difference $I_2 - I_1$ is relatively constant, equalling 0.583 ± 0.002 in this case. Thus the data suggest that at quasi-steady state

$$I_2 \approx I_1 + 0.6, \qquad \gamma \ll 1 \tag{69}$$

for reasons not readily apparent.

Figure 7 is a plot of the magnitude $|\partial f/\partial n|$ of the dimensionless normal derivative at the electrode surface at various times T vs. angle θ, for $\gamma = 0.009983$. The solid curve is the one-dimensional gradient given by eqn. (5), whereas the points represent $\partial f/\partial n$ values determined numerically. Prior to overlap of the electrodes'

TABLE 2
Absolute and relative errors between I_1 and I_2 values determined by equating $\partial f/\partial T$ to zero. I_1 was computed from eqn. (6)

γ	I_1	I_2	$(I_2 - I_1)/I_1$	$I_2 - I_1$
5×10^{-6}	12.899	13.480	0.0431	0.581
1×10^{-5}	12.206	12.788	0.0455	0.582
5×10^{-5}	10.597	11.179	0.0521	0.582
0.0001	9.904	10.487	0.0556	0.583
0.001	7.601	8.185	0.0713	0.584
0.002	6.909	7.495	0.0782	0.586

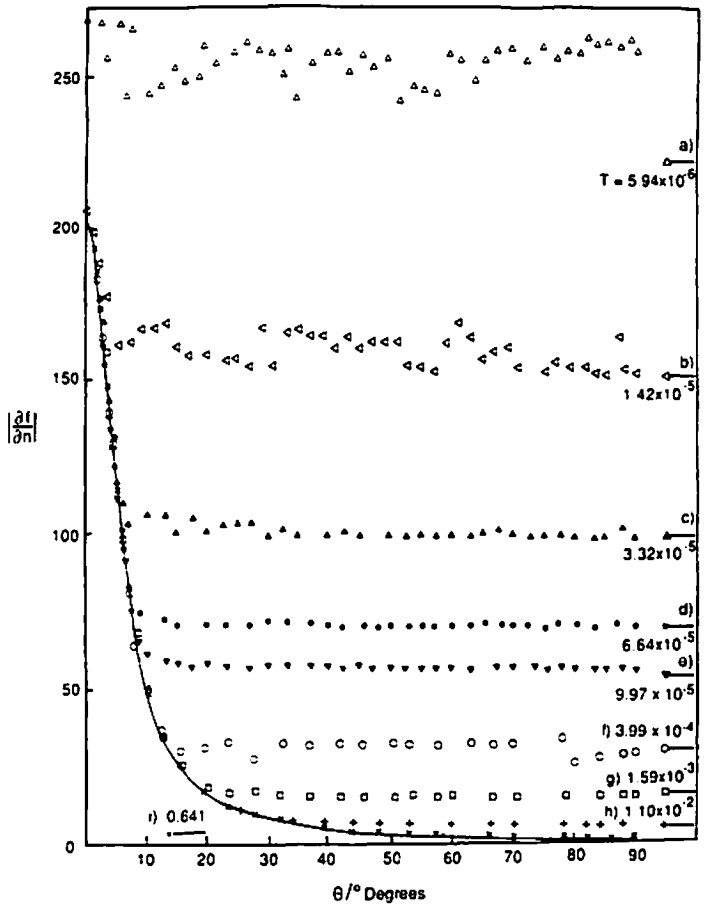

Fig. 7. Plot of $|\partial f/\partial n|$ vs. θ for $\gamma = 0.009983$ and various T. Solid curve is given by eqn. (5); points represent numerical data. The horizontal bars on the right-hand side represent $|\partial f/\partial n|$, as calculated from eqn. (68).

diffusion layers, $\partial f/\partial n$ is independent of θ and equals approximately the spherical gradient given by eqn. (68), as argued above (curve a; some discretization error at this short time is apparent). As the diffusion layers overlap increasingly at later times, the computations show that $\partial f/\partial n$ is well approximated by the one-dimensional gradient over an increasingly large θ range (curves b–h). This behavior is not surprising for small θ but is somewhat unexpected for the larger θ values. For very large θ, however, $\partial f/\partial n$ does not diverge from the spherical gradient, because the diffusion layers have not yet overlapped in the large fraction of solution not near both hemispheres. As T increases further and I_2 approaches a quasi-steady-state value, $\partial f/\partial n$ for all θ is closely approximated by the one-dimensional gradient (curve i). (Note that I_2 ($T = 0.0110$) and I_2 ($T = 0.641$) in Fig. 6 are substantially

different, even though the corresponding concentration gradients in Fig. 7 are quite similar. This apparent discrepancy exists because the bulk of the electrode area is associated with large θ values.)

Thus, to a first approximation, this thin layer cell and its surrounding solution volume effectively behave (at least for small γ) as if composed of two regions. The first is a small cylindrical region, whose volume increases with time, that is centered about the z (or ϵ) axis and in which the current is attributable principally to one-dimensional axial diffusion. The second is the surrounding peripheral region, in which the current is attributable principally to radial diffusion. These observations furthermore suggest a means for approximating I_2 analytically when $\gamma \ll 1$. Prior to the time T_0 of diffusion-layer overlap, I_2 can be approximated by eqn. (68). For times $T \geqslant T_0$, eqn. (5) gives approximately the current in the central cylindrical region, if integrated from $\theta = 0$ to $\theta = \theta_T$, where θ_T is determined by the intersection of the two functions describing the one-dimensional and spherical concentration gradients

$$\frac{1}{(\pi T)^{1/2}} + 1 = \frac{2}{\gamma + 2(1 - \cos \theta_T)} \tag{70}$$

or where

$$\cos \theta_T = \frac{1}{2}\left(\frac{2}{(\pi T)^{1/2} + 1} + \gamma\right), \qquad T_0 \leqslant T < \infty \tag{71}$$

Furthermore, eqn. (68), multiplied by $\cos \theta_T$, describes approximately the current in the surrounding peripheral region. The factor $\cos \theta_T$, the ratio of the surface area of this peripheral electrode region to that of the hemisphere, corrects for the reduced electrode area. The twin hemispherical cell current is then approximated by summing these currents. The result is

$$I_2 \approx \frac{1}{(\pi T)^{1/2}} + 1 + U_{T_0}\left(\ln(1 + 2(1 - \cos \theta_T)/\gamma) + \left(\frac{1}{(\pi T)^{1/2}} + 1\right)(\cos \theta_T - 1)\right)$$
$$\gamma \ll 1 \tag{72}$$

where U_{T_0} is the Heaviside (unit) step function, equalling 0 when $T < T_0$ and 1 when $T \geqslant T_0$. Quantity T_0 is determined by setting $\theta_T = 0$ in eqn. (70) and solving for T

$$T_0 = \frac{1}{\pi}\left(\frac{\gamma}{2 - \gamma}\right)^2 \approx \frac{\gamma^2}{4\pi} \qquad \gamma \ll 1 \tag{73}$$

The dashed curves in Fig. 6 are plots of eqn. (72) for the two smallest γ values. The agreement between eqn. (72) and the numerical results is especially good at short times, when θ_T and the central cell volume are small. As T and θ_T increase, however, the approximation $\partial^2 c/\partial z^2 = 0$ in the central region of the cell becomes poorer and the curves diverge.

The finding that the twin hemispherical cell effectively behaves as a stack of numerous parallel-plate electrodes is somewhat non-intuitive when γ is small. Because the radius R of curvature is much greater than the separation distance r_0 in this case, the two electrodes resemble parallel plates in the vicinity of $\theta = 0$, where $\partial f/\partial n$ is the largest. One might consequently anticipate that the current would be localized entirely in this plate-like region. The current at any thin circular strip, however, is proportional to $(\partial f/\partial n) \sin \theta$ (see eqns. 5 and 41), which reaches a maximum value for some $\theta > 0$. (For example, the one-dimensional model predicts that the current Δi is largest at the strips for which $\theta = 5.7°$ and $11.7°$ when $\gamma = 0.009983$ and 0.04219, respectively.) The factor $\sin \theta$ weights the normal derivative because the strip area increases with angle θ. Hence the current is not restricted to the $\theta = 0$ region but is also significant in the immediately surrounding region. The cell consequently does not behave as a single set of two parallel plates separated by r_0.

Although the numerical solution of eqn. (25) was simplified by considering only the limiting case in which $D_0 = D_R$ and $c_O^* = c_R^*$, the results reported here, if properly corrected, should also apply to less specific cases. In general, the steady-state diffusion-limited current generated at two parallel-plate electrodes by a redox couple, the constituents of which have unequal diffusion coefficients and are present in unequal concentrations, is given by eqn. (2), with D replaced by $D_O D_R/(D_O + D_R)$ and c^* replaced by $c_O^* + c_R^*$ [1]. Because the hemispherical cell behaves as a contiguous stack of parallel-plate electrodes, the substitution of the above formulae for D and c^* in the steady-state I_2 expression should similarly correct the data presented here.

CONCLUSIONS

The numerical results presented above show that the diffusion-limited current expected at a thin layer cell constructed from two hemispherical electrodes can be predicted to within 10% by eqn. (6), if the distance between the electrodes is less than one-hundredth of the hemisphere radius. From these results some tentative conclusions are now drawn regarding the applicability of one-dimensional fluxes to and currents at other thin layer cells, such as the ones shown in Fig. 2.

Of these alternative geometries, the twin conical cell most closely resembles the model problem. The importance of radial diffusion in this case can be judged principally by the aspect ratio α. As $\alpha \rightarrow \infty$, the cone collapses into a disk, to which radial diffusion is small for a conventionally sized electrode (because $\overrightarrow{dA}$ and $\vec{J}_r$ are orthogonal). As $\alpha \rightarrow 0$, the cone approaches an infinite cylinder, at which a decaying transient is expected due to cylindrical diffusion [13]. Since the radial flux to the hemispherical cell is relatively constant for $T > \sim 1$ but does not perturb I_2 significantly from I_1, it is unlikely that this transient alone will have a significant effect. Cells characterized by intermediate α values most likely behave similarly. The one-dimensional current at the twin conical cell is thus expected to be roughly comparable in accuracy to that for the hemispherical cell.

The currents generated by thin layer cells formed from a hemisphere and a plane, and a cone and a plane, should be more accurately described by one-dimensional fluxes than currents generated by twin conical and hemispherical cells, because the radial flux is perpendicular to the planar electrode and can only augment the axial flux to this electrode. The equations for these cells should thus be valid whenever the conical and hemispherical equations are acceptably accurate.

The electrode area of the crossed-cylinder cell depicted in Fig. 1 is smaller than that of two hemispheres of equivalent radius, and the cell does not deplete electroactive species from a hemispherical solution volume by radial diffusion, as does the hemispherical cell, but from a smaller volume. In the light of the above arguments, a one-dimensional flux is also expected for this case. A further study of the flux to the electrodes of this cell is underway.

Thus a cautious interpretation of the results contained herein suggests that currents generated by thin layer cells in which the electrodes are separated by very short distances can be approximated by considering only the axial flux to the electrode surface. Because the diffusive currents at these cells can be modeled simply, such cells may well prove useful in studying solution and charge-transfer kinetics.

GLOSSARY

a, b, d, g	scaling factors for computation of spatial derivatives
c^*	bulk concentration of Ox or Red
c_O^*	bulk concentration of Ox
c_R^*	bulk concentration of Red
c_O	concentration of Ox
c_R	concentration of Red
dA	differential area
D	diffusion coefficient of Ox or Red
D_O	diffusion coefficient of Ox
D_R	diffusion coefficient of Red
DMA	dimensionless time between successive iterations
f	$c_O/c_O^* = c_O/c^*$
f_0	center point of five-star network
f_A, f_B, f_D, f_G	surrounding points of five-star network
F	function defined by eqn. (50)
G	function defined by eqn. (51)
H	function defined by eqn. (52)
i_d	current at spherical electrode
I_1	dimensionless one-dimensional steady-state current
I_2	dimensionless two-dimensional current
$I_{2\infty}$	limiting I_2 values as $\gamma \rightarrow \infty$
$\vec{J}$	vector sum $\vec{J}_r$ and $\vec{J}_z$
$\vec{J}_r$	radial flux vector

$\vec{J}_z$	axial flux vector
l	separation between parallel-plate electrodes
nF	Charge number of reaction multiplied by Faraday's constant
Ox	oxidized forms of redox couple
r	radial coordinate
$\vec{r}$	radial unit vector
r_0	separation distance between electrodes of thin layer cell
R	half-sphere radius
Red	reduced form of redox couple
t	time
T	Dt/R^2
T_0	dimensionless time defined by eqn. (73)
U_{T_0}	unit step function
X	$\zeta/\Delta\zeta$
z	axial coordinate
$\vec{z}$	axial unit vector
$\partial f/\partial n$	dimensionless concentration gradient
α	conical aspect ratio
γ	r_0/R
ΔA	area of circular strip
Δi	current at ΔA
ΔT	$D\,\Delta t/R^2$
$\Delta\epsilon$	minimum grid spacing in ϵ direction
$\Delta\zeta$	minimum grid spacing in ζ direction
ϵ	z/R
ζ	r/R
θ	angle defined in Fig. 2b
θ_T	angle defined by eqn. (71)
Φ	function describing solution volume
Φ_1	function describing surface area of upper hemisphere
Φ_2	function describing surface area of lower hemisphere
Φ'	dimensionless function describing solution volume
Φ_1'	dimensionless function describing surface area of upper hemisphere

ACKNOWLEDGEMENT

This work was supported by the Welch Foundation Grant F079 and the National Science Foundation Grant CHE-8402135. The authors thank S.W. Feldberg (of Brookhaven National Laboratory) for helpful discussions.

REFERENCES

1 A.T. Hubbard and F.C. Anson, in A.J. Bard (Ed.), Electroanalytical Chemistry Vol. 4, Marcel Dekker, New York, 1970, p. 129.

2 F.-R.F. Fan and A.J. Bard, J. Am. Chem. Soc., in press.
3 G.P. Kittlesen, H.S. White and M.S. Wrighton, J. Am. Chem. Soc. 106 (1984) 7389.
4 C.E. Chidsey, B.J. Feldman, C. Lundgren and R.W. Murray, Anal. Chem., 58 (1986) 601.
5 T. Joslin and D. Pletcher, J. Electroanal. Chem., 49 (1974) 171.
6 S.W. Feldberg, J. Electroanal. Chem., 127 (1974) 171.
7 L. Fox, Numerical Solution of Ordinary and Partial Differential Equations, Pergamon, New York, 1962.
8 G.E. Forsythe and W.R. Wasow, Finite-Difference Methods for Partial Differential Equations, Wiley, New York, 1960.
9 G.D. Smith, Numerical Solution of Partial Differential Equations, 2nd ed., Clarendon, Oxford, 1978.
10 R.V. Viswanathan, Mathematical Tables and Aids to Computation, 1957, pp. 11, 67.
11 S.W. Feldberg, personal communication, February 1987.
12 A.J. Bard and L.R. Faulkner, Electrochemical Methods, Wiley, New York, 1980.
13 P. Delahay, New Instrumental Methods in Electrochemistry, Interscience, New York, 1954.